

Cite this: *J. Mater. Chem. A*, 2019, 7, 6080

Overall structural modification of a layered Ni-rich cathode for enhanced cycling stability and rate capability at high voltage†

Manjing Tang,^a Jun Yang,^a ^{*a} Nantao Chen,^a Shengcai Zhu,^{*b} Xing Wang,^a Tian Wang,^a Congcong Zhang ^c and Yongyao Xia ^{*c}

The vital challenge in relation to layered Ni-rich cathodes is their pronounced structural degradation originating from cation mixing at high voltage, which causes serious electrode polarization and electrochemical deterioration. Herein, an overall structural modification strategy, which integrates a Li_2GeO_3 coating with gradient Ge-doping, was developed to improve the structural stability and create ordered diffusion channels in a layered Ni-rich cathode *via* interfacial fusion at high temperature. This effective strategy significantly enhances the reversible capacity retention, voltage stability and rate capability of the layered Ni-rich cathode at high voltage. We find that the Li_2GeO_3 coating inhibits interfacial side reactions to enhance the surface structural stability of the cathode materials. More importantly, the gradient Ge-doping plays a critical role in suppressing cation mixing to improve the ordered channels available for Li^+ ion transport. The experimental observations, corroborated by first principle calculations, further reveal that Ge-doping not only alleviates structural degradation by increasing the phase transition energy barrier for layers to form spinel-like or rock-salt phases, but also facilitates fast Li^+ diffusion kinetics *via* reducing the diffusion barrier. Our work provides a design idea for stabilizing the surface/bulk structure of advanced cathodes for high-performance Li-ion batteries.

Received 28th December 2018
Accepted 13th February 2019

DOI: 10.1039/c8ta12494a

rsc.li/materials-a

1. Introduction

Recently, lithium-ion batteries (LIBs) have attracted great attention as renewable and high-efficiency energy storage systems with a wide range of applications, such as in portable electronics, smart power stations and electric vehicles.^{1,2} With growing demand for LIBs, it is urgent to exceed current battery performance levels to meet the requirements and developments necessary for energy-storage applications. In particular, practical LIBs used for powering electric vehicles should have high energy and power densities. In this regard, layered Ni-rich oxides, such as $\text{LiNi}_{0.8}\text{Co}_{0.1}\text{Mn}_{0.1}\text{O}_2$, are promising cathode materials, due to their high reversible capacity (200 mA h g^{-1}) and low cost.^{3,4} However, layered Ni-rich cathodes have the fatal

drawback of inherent structural instability, which seriously hinders their commercial application.^{5,6} The poor structural stability is closely related to $\text{Li}^+/\text{Ni}^{2+}$ cation mixing, because of the similar radii of Li^+ (0.076 nm) and Ni^{2+} (0.069 nm), which inevitably occurs in Ni-rich oxides during preparation and application.^{7,8} In such a disordered phase following cation mixing, Ni^{2+} located at Li sites greatly increases the Li^+ ion diffusion kinetic barrier. In particular, at high voltages, the highly active surface of the delithiated cathode can trigger the decomposition of the electrolyte, forming a thick solid-electrolyte interface (SEI) layer. Even worse, interfacial reactions cause high-valence Ni^{4+} ions to be reduced to Ni^{2+} ions and then migrate to Li layers, resulting in the formation of disordered spinel-like and/or rock-salt phases.^{9–13} The thick SEI layer and severe cation mixing phase can greatly increase the electrode interfacial resistance, passivating Li^+ ion diffusivity and leading to the drastic deterioration of electrochemical performance.

Extensive studies have been conducted to improve the electrochemical performance of layered Ni-rich cathodes through suppressing cation mixing.^{14–16} As a common modification strategy, surface coatings can effectively isolate active materials from the electrolyte to prevent serious side reactions.^{17–19} Reported works have shown that the compounds selected as coating materials should be endowed with outstanding electrochemical stability to realize the stabilization of the electrode/

^aSchool of Materials Science & Engineering, Shaanxi Key Laboratory of Green Preparation and Functionalization for Inorganic Materials, Shaanxi University of Science & Technology, Xi'an, Shaanxi 710021, People's Republic of China. E-mail: yangjun1561@163.com

^bCenter for High Pressure Science and Technology Advanced Research (HPSTAR), Shanghai 201203, P.R. China. E-mail: shengcai.zhu@hpstar.ac.cn

^cDepartment of Chemistry, Shanghai Key Laboratory of Molecular Catalysis and Innovative Materials, Institute of New Energy, Fudan University, Collaborative Innovation Center of Chemistry for Energy Materials, Shanghai 200433, People's Republic of China. E-mail: yxyxia@fudan.edu.cn

† Electronic supplementary information (ESI) available. See DOI: 10.1039/c8ta12494a

electrolyte interface.^{17–20} Although surface coating can resolve surface structural degradation, concomitantly, unavoidable cation mixing resulting from metal ion migration in the bulk at high voltage intensively limits any improvement. To overcome this problem, lattice doping is considered an effective strategy to regulate the crystal structure and improve the bulk structural stability.^{21–24} However, surface structural degradation remains a serious problem in doped materials when operating at high voltage.²⁵ Therefore, in order to fundamentally solve the structural instability problems related to Ni-rich oxide cathodes, it is essential to holistically consider structural modification from surface to bulk. However, current methods have a limited effect in terms of integrating coating and doping in the cathode material. Additionally, it is also a great challenge to avoid Ni³⁺ reduction and disordered phase formation at the interfaces of coated cathodes.^{22,26}

Inspired by ion diffusion at heterogeneous interfaces under high temperature,²⁷ we develop an overall structural modification method from surface to bulk through interfacial fusion during the co-lithiation of GeO₂-coated precursors. This strategy masterfully integrates a surface Li₂GeO₃ coating and bulk Ge-doping in a Ni-rich cathode. The electrochemically stable Li₂GeO₃ coating can inhibit adverse interfacial side reactions to enhance surface structural stability. More surprisingly, Ge-doping significantly reduces Li⁺/Ni²⁺ cation mixing (to a low amount of 0.223%), improving the availability of ordered channels for Li⁺ ion transport, which is far different from reported work that has suggested that doping may induce Ni³⁺ reduction and disordered phase formation at the heterogeneous interface of the coated cathode.^{22,28,29} Furthermore, first principles calculations clarify these outstanding effects of Ge-doping on the structure of the Ni-rich cathode, indicating that Ge-doping not only alleviates structural degradation *via* increasing the phase transition energy barrier for layers to form spinel-like/rock-salt phases, but it also facilitates fast Li⁺ diffusion kinetics *via* reducing the diffusion barrier. With the overall structural modification integrating coating and doping, as expected, the modified Ni-rich cathode exhibits enhanced reversible capacity retention, voltage stability and rate capability compared with a pristine example at high voltage (4.5 V).

2. Experimental and computational section

2.1. Materials preparation

The pristine layered Ni-rich cathode was synthesized *via* a solid-state reaction.^{23,25} The Ni_{0.82}Co_{0.12}Mn_{0.06}(OH)₂ precursor was mixed with LiOH·H₂O at the appropriate molar ratio, and excess 5 mol% Li was added to compensate for the evaporation of Li salt at high temperature. Then, the mixture was sintered at 480 °C and 800 °C under an O₂ flow for 5 and 12 h, respectively. The obtained cathode material was denoted as NCM811. For preparing germanium oxide-coated precursors (Ni_{0.82}Co_{0.12}Mn_{0.06}(OH)₂@GeO₂), GeO₂ powder was dissolved in ethanol solution with ammonia, and then the Ni_{0.82}Co_{0.12}Mn_{0.06}(OH)₂ precursor was added into the solution to form a uniform

dispersion. Afterwards, the mixed solution was vigorously stirred at 80 °C until the solvent completely evaporated. The GeO₂-coated precursor was mixed with LiOH·H₂O and then sintered *via* the same process as for NCM811. The as-prepared modified cathode was denoted as NCM811@LGO.

2.2. Materials characterization

Powder X-ray diffraction (XRD, Bruker D8 Advance) measurements, using Cu K α radiation, were carried out to determine the crystal structures and phases of the samples. Rietveld refinement was carried out to analyze the refined structural parameters using the TOPAS software package. The surface morphologies and micro-regional structures of the samples were observed using a scanning electron microscope (SEM, Hitachi S4800) and transmission electron microscope (TEM, FEI Tecnai G2 F20 S-TWIN). The elemental distributions in the samples were investigated *via* energy dispersive spectroscopy (EDS) mapping analysis. The elemental compositions of the materials were determined using an inductively coupled plasma atomic emission spectrometer (ICP-AES). Surface compositions and valences were analyzed *via* X-ray photoelectron spectroscopy (XPS, AXIS SUPRA). In addition, Ar-ion etching was performed to obtain depth-dependent elemental distribution and valence information from samples.

2.3. Electrochemical measurements

Electrochemical performance was measured using coin-type CR2016 cells. To prepare the cathode, active material, carbon black, and polyvinylidene difluoride (PVDF) were mixed in *N*-methyl-2-pyrrolidone (NMP) solvent at a weight ratio of 8 : 1 : 1. Then, the slurry was cast onto an aluminum-foil current collector, followed by drying at 80 °C for 12 h under vacuum. The electrode film was pressed and punched into disks with a diameter of 12 mm. Cells were assembled, with the as-prepared cathode, lithium metal as the anode, and Celgard 2300 film as the separator, in a box filled with pure argon. The electrolyte solution was 1 M LiPF₆ dissolved in EC/DMC/EMC (1 : 1 : 1 by volume). Galvanostatic charge–discharge experiments were performed between 2.0 and 4.5 V vs. Li/Li⁺ at room temperature (25 °C) with a LAND CT2001A battery cycler (Wuhan, China). Electrochemical impedance spectroscopy (EIS) measurements were conducted using a PARSTAT MC electrochemical system (Princeton Applied Research, USA) over the frequency range of 1 MHz to 1 mHz, with an AC amplitude of 5 mV at room temperature. Galvanostatic intermittent titration technique (GITT) measurements were carried out by charging the half-cells at a C/10 current to different voltages followed by open circuit relaxation for 120 min.

2.4. Computational methods

We employ a recently developed stochastic surface walking (SSW) method integrated with density functional theory (DFT) for crystal sampling to clarify the mechanism of phase transition. The details of the algorithm used for SSW pathway sampling are described in previous works.^{30–33} The SSW pathway sampling is fully automated and divided into three stages in

simulation: (i) utilizing the SSW method to explore all likely phases near the phase; (ii) utilizing the variable-cell double-ended surface walking (DESW) method to establish a pseudo-pathway connecting ISs (intermediate states) to FSs (free states) for all IS/FS pairs; and (iii) locating exactly the transition states (TSs) of the candidate lowest energy pathways using the DESW TS-search method.³⁴ Based on the sampled free energy landscape, the pathways connecting the initial structure and final structure on the potential energy surface can be determined *via* atom-to-atom correspondence. This approach has been recently utilized to investigate the mechanism of phase transition in other materials.^{30–33} The SSW-crystal method was carried out using the plane wave density functional theory program Vienna *ab initio* simulation package (VASP), where the electron-ion interactions of Ni, O, Ge and Li atoms are represented using the projector augmented wave scheme.³⁵ The exchange–correlation functional is described *via* the generalized gradient approximation (GGA) with Perdew–Burke–Ernzerhof (PBE) parameterization.³⁶ The pathway sampling was carried out in a 16-atom (4 NiO₂ units per cell) lattice. Through exhaustive SSW sampling, a large set (in the order of 10³) of initial/final state pairs was collected. We located the TS *via* the double-ended surface walking approach and refined candidate pathways through sorting the heights of computed energy barriers. For the Li⁺ ion diffusion energy barrier, calculations were performed using a modest 1 × 1 × 1 *k*-point grid set, due to the large supercells employed (~200 atoms), which was generated *via* a Monkhorst–Pack scheme.³⁷ Dispersion corrections have been shown to be important in the prediction of the lattice parameters of layered cathode materials. In order to account for the van der Waals (vdW) interactions, we incorporated dispersion corrections using the optPBE functional.³⁸

3. Results and discussion

3.1. Structural analysis of a Ni-rich cathode modified by surface coating and bulk doping

A layered Ni-rich cathode (NCM811) was synthesized through sintering precursors with Li salt at 800 °C. The modified Ni-rich cathode (NCM811@LGO), integrating surface coating with bulk doping, is fabricated *via* the co-lithiation of pre-coated precursors. During the sintering process for the GeO₂-coated precursors, as schematically illustrated in Fig. 1a, Li⁺ ion diffusion promotes the *in situ* formation of Li₂GeO₃ coating layers on the Ni-rich cathode surface. Simultaneously, at the heterogeneous interface between the coating layers and cathode, some Ge⁴⁺ ions diffuse into the Ni-rich cathode to generate a gradient doping structure. The surface morphologies of the modified and pristine samples were studied *via* scanning electron microscopy (SEM). Both samples show dense spherical secondary particles of ~20 μm (Fig. 1b and c), tightly assembled from primary crystallites (Fig. 1d and e). The samples show no obvious changes in surface morphology and crystallinity after structural modification. Interestingly, the modified sample (Fig. 1e) exhibits the rough surface of a primary crystal compared with the pristine sample (Fig. 1d), implying the presence of a thin coating layer on NCM811. The component

elements are uniformly distributed throughout the entire secondary microspheres (Fig. S1†). Furthermore, high-resolution transmission electron microscopy (TEM) measurements were conducted to observe and analyze the micro-regional surfaces/interfacial structures of the as-prepared materials. As shown in Fig. 1f, the pristine cathode presents a well-defined layered structure from surface to bulk, and the lattice distance of 0.47 nm is assigned to the (003) crystal facet of the rhombohedral phase, which is identified *via* FFT (Fig. 1h). In the modified sample shown in Fig. 1g, a thin nanolayer of ~6 nm is uniformly and tightly coated on the surface of NCM811. The lattice fringes from the surface (0.24 nm) and bulk phase (0.47 nm) can be clearly observed and assigned to the (002) plane of Li₂GeO₃ and the (003) plane of NCM811, as evidenced by FFT (Fig. 1i). In the micro-region indicated by the green rectangle in Fig. 1j, TEM-EDS mapping shows a homogeneous distribution of Ni, Co, Mn and Ge elements in the modified primary particle (Fig. 1k). Surprisingly, the line scan (indicated by the red arrow in Fig. 1j) shows that the Ge elements present a gradient-reduced distribution from surface to bulk in the modified particles (Fig. 1l), which is very different from the distribution of Ni, Co and Mn elements (Fig. S2†). This result implies that Ge⁴⁺ ions from the coating layers are doped in gradient form in the modified cathode.

X-ray photoelectron spectroscopy (XPS) can be utilized to analyze the element valences in materials. Notably, the peak positions of Ni 2p (Fig. 2a) and Co 2p (Fig. 2b) for the modified sample have slightly shifted compared with the pristine sample, indicating that the valence states of Ni and Co are influenced by Ge⁴⁺ doping. The Ni 2p_{3/2} peak position for the modified sample is observed at 855.4 eV, higher than that for the pristine sample (854.6 eV), suggesting the presence of more Ni³⁺ ions near the surface.³⁹ Hence, it is reasonable to speculate that the partial oxidation of Ni²⁺ into Ni³⁺ ions is induced by Ge⁴⁺ lattice doping, which is beneficial for reducing Li⁺/Ni²⁺ cation mixing. Meanwhile, the shift to a higher binding energy of the Co 2p_{3/2} peak for the coated sample may be ascribed to the transformation of ions from Co³⁺ to Co²⁺ to compensate for the increased valance of Ni²⁺ ions, consistent with the reported literature.^{40–42} To further determine the influence of Ge element distribution on the valances of Ni and Co, depth-dependent XPS spectra of Ge, Ni and Co elements were measured after different etching times. Fig. 2c shows that the peak intensity of the Ge 3d spectrum decreases with increased etching time, confirming the gradient distribution of Ge elements in the modified sample.^{42,43} Moreover, the oxidation states of Ni ions are affected by the Ge-doping content; as shown in Fig. 2d, the high-content Ge region close to the surface facilitates the formation of high-valence Ni³⁺ ions. Conversely, a lower Co²⁺ ion content exists in the region with a higher Ge content (Fig. S3†). Therefore, it is concluded from these results that the gradient Ge-doping results in Ni ions with an increased oxidation state, while the valence state of Co ions is reduced to maintain charge balance.

In order to investigate the influence of this lattice doping on the crystal structure of NCM811, XRD patterns of the as-prepared samples were recorded and are shown in Fig. 2e. All

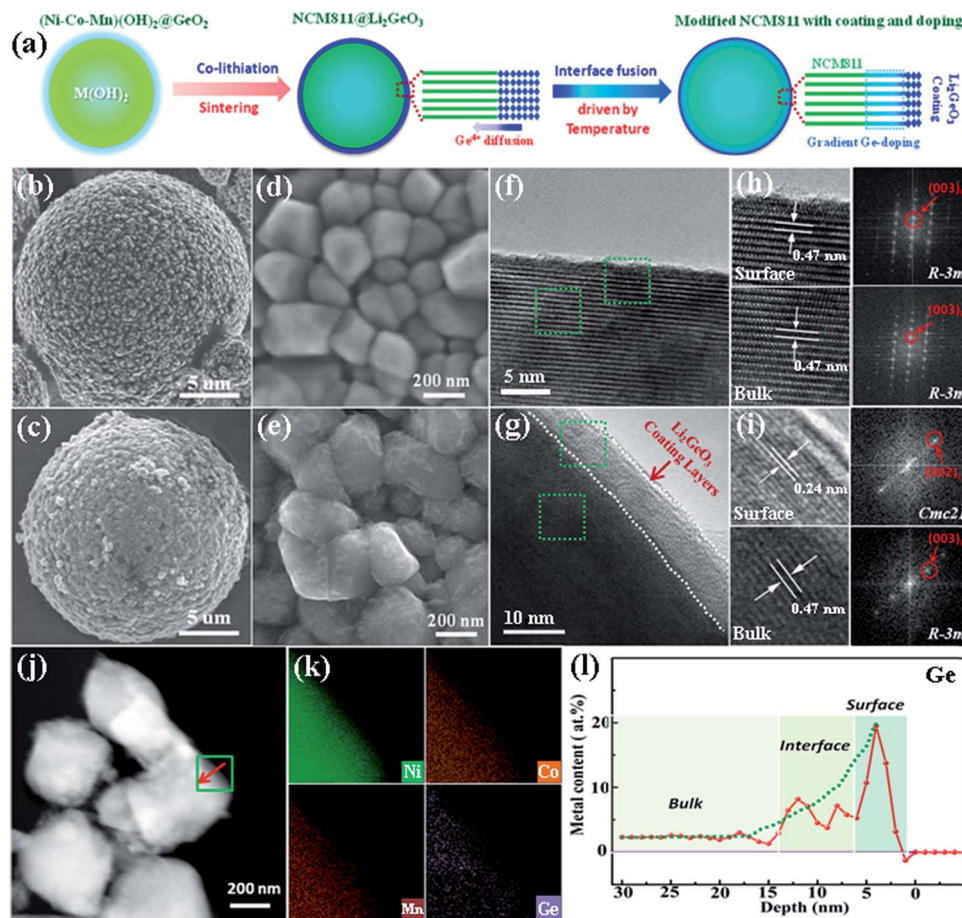


Fig. 1 (a) A schematic illustration of the formation of the Li_2GeO_3 coating layer and the gradient doping structure on a Ni-rich cathode particle; SEM, HRTEM and FFT images of (b, d, f, h) NCM811 and (c, e, g, i) NCM811@LGO; and (j, k) EDS mapping and (l) a line scan of Ge elements in NCM811@LGO.

diffraction peak profiles from the as-prepared samples could be indexed to a layered hexagonal $\alpha\text{-NaFeO}_2$ -type structure with the space group $R\bar{3}m$. Interestingly, the splitting into (006)/(012) and (108)/(110) doublets shown by the modified sample becomes more obvious compared with NCM811 (inset of Fig. 2e), revealing the improved degree of order of the layered structure in the modified sample.⁴⁴ In addition, the (006) diffraction peak of NCM811@LGO shifts to a lower angle, and the (110) diffraction peak shifts to a higher angle compared with NCM811, which is a result of an expanded c axis and a contracted a axis. The crystal structures of the samples are further analyzed *via* Rietveld refinement based on the space group $R\bar{3}m$ (Fig. 2f). The corresponding analysis results (Table 1) indicate that the lattice parameter c increases, while a slightly decreases in the modified sample. It is well accepted that the I_{003}/I_{104} and c/a ratios can provide information related to the degree of $\text{Li}^+/\text{Ni}^{2+}$ cation mixing.^{23,39} XRD analysis results show that the I_{003}/I_{104} and c/a ratios for the modified sample remarkably increase *versus* those of the pristine sample (Table 1), indicating that the modified sample has significantly reduced $\text{Li}^+/\text{Ni}^{2+}$ cation mixing (0.223%) compared with NCM811 (3.021%), which is closely related to the higher $\text{Ni}^{3+}/\text{Ni}^{2+}$ ratio demonstrated by the XPS

results (Fig. 2a). Therefore, the above results reveal that lattice doping plays a positive role in maintaining the crystal structure. In particular, reduced cation mixing means that the modified sample can provide more ordered channels for fast Li^+ ion diffusion, which is beneficial for promoting the electrochemical performance of the cathode.

3.2. Enhanced electrochemical performance of the modified Ni-rich cathode

To evaluate the electrochemical performance of the cathodes at high voltage, the half-cells were cycled at 2.0–4.5 V. Simultaneously, the electrochemical stability of Li_2GeO_3 prepared through a solid-state method was also evaluated *via* cyclic voltammetry. From Fig. S4,[†] we can find that Li_2GeO_3 presents excellent structural stability under the voltage used. The initial charge–discharge curves at 0.1C (20 mA g^{-1}) are shown in Fig. S5a;[†] the charge/discharge capacities of NCM811 and NCM811@LGO are 234.2/202.1 mA h g^{-1} and 238.7/208.6 mA h g^{-1} , respectively. Remarkably, the NCM811@LGO cathode exhibits a lower onset potential for delithiation during initial charging compared with NCM811 (Fig. S5a and S5b[†]), which is a benefit of the reduced $\text{Li}^+/\text{Ni}^{2+}$ cation mixing. The

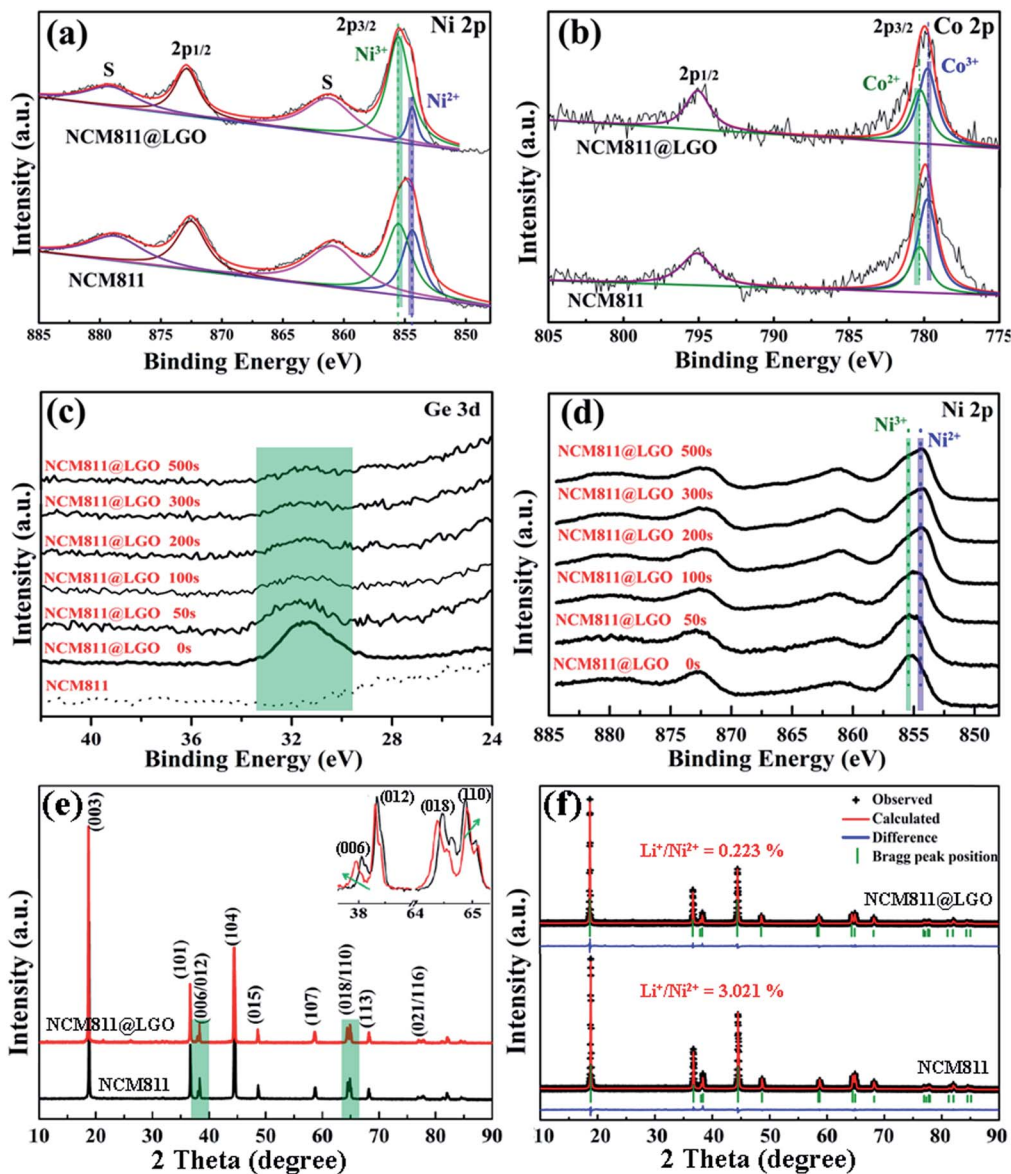


Fig. 2 (a) Ni 2p and (b) Co 2p XPS spectra from the as-prepared samples; and depth-dependent (c) Ge 3d and (d) Ni 2p spectra from NCM811@LGO at different etching times. (e) XRD patterns and (f) Rietveld refinements of the as-prepared samples.

cycle-life test results (Fig. 3a) show that the reversible capacity of NCM811@LGO still maintains 81% of its initial capacity after 100 cycles, but NCM811 retains only 54%. In addition, as shown in Fig. 3b, it can be found that NCM811 shows obvious variations in its charge/discharge profiles over an extended number of cycles, along with a rapid decline in capacity. This indicates that the electrode polarization caused by the structural

degradation of NCM811 becomes more serious during high-voltage cycling.²⁵ However, this polarization phenomenon can be effectively suppressed in NCM811@LGO, which retains similar charge-discharge profiles and undergoes slower capacity decay (Fig. 3c). The average discharge voltage is also highly influenced by electrode polarization during high-voltage cycling (Fig. 3d). Evidently, the discharge voltage of NCM811

Table 1 Crystal structural parameters of the as-prepared cathodes powders

Sample	<i>a</i> (Å)	<i>c</i> (Å)	Volume (Å ³)	<i>c/a</i>	<i>I</i> ₀₀₃ / <i>I</i> ₀₀₄	Ni ²⁺ in Li layers (%)	<i>R</i> _{wp} (%)	<i>R</i> _p (%)
NCM811	2.87524	14.20346	101.68908	4.93992	1.70	3.021	3.88	2.98
NCM811@LGO	2.87094	14.21707	101.48226	4.95206	2.20	0.223	4.58	3.47

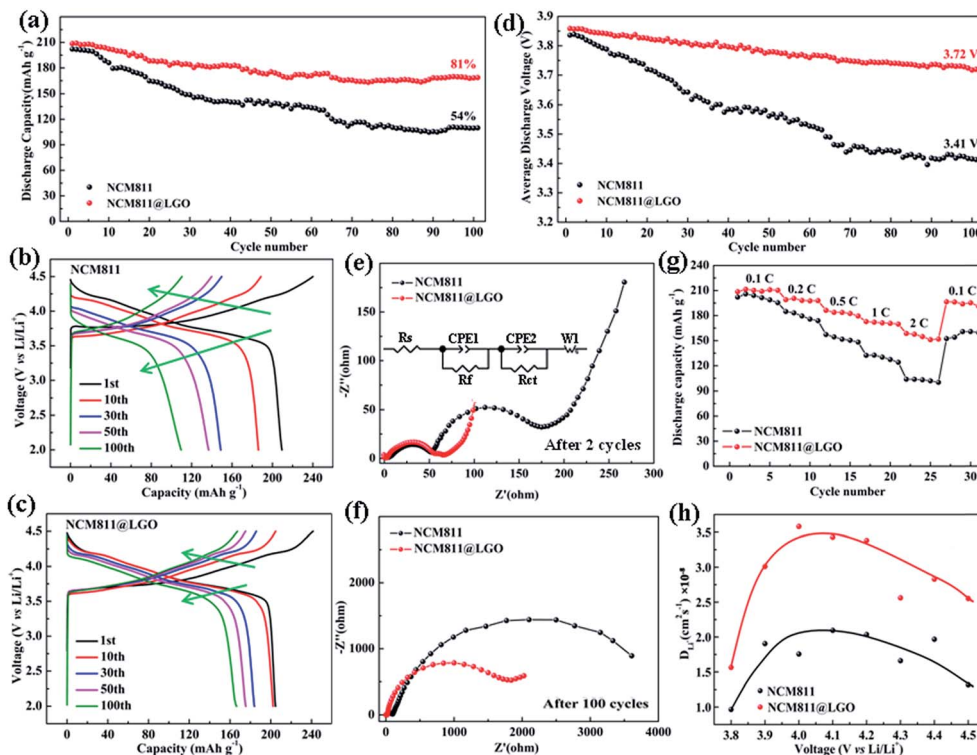


Fig. 3 The cycling stability of the as-prepared cathodes: (a) the discharge capacities, (b, c) charge–discharge profiles and (d) the average discharge voltages of the cathodes between 2.0 and 4.5 V vs. Li/Li⁺ at 0.1C. (e, f) Nyquist plots of the electrodes after high-voltage cycling. (g) Discharge capacities of the as-prepared cathodes at different rates. (h) Li⁺ ion diffusion coefficients of the cathodes during the first charging process.

rapidly falls from 3.84 V to 3.41 V after 100 cycles, but NCM811@LGO exhibits a significantly steady discharge voltage (from 3.85 to 3.72 V) during cycling. Moreover, the differential capacity curves (Fig. S5c and S5d[†]) clearly demonstrate the effects of electrode polarization on the charge/discharge voltage. The potential shifts and peak area reduction of redox peaks caused by electrode polarization are hugely alleviated in NCM811@LGO. Furthermore, long-term charge/discharge cycle testing at a high current density (200 mA g⁻¹) indicates that NCM811@LGO still presents excellent cycling stability compared with NCM811 (Fig. S6[†]). The improved cycling life of the NCM811@LGO cathode is directly correlated with the enhanced electrode structural stability, which is contributed to by Li₂GeO₃ acting as protecting layers, avoiding surface structural deterioration, and Ge-doping suppressing phase transitions during high-voltage cycling. To reveal the relationship between structural degradation and the electrode interface resistance, electrochemical impedance spectroscopy (EIS) studies were performed on an electrode charged to 4.3 V after 2 and 100 cycles. After the initial cycle (Fig. 3e), the plots are composed of two semicircles in the high-frequency region and a slope in the low-frequency region. The semicircle at the higher frequency is assigned to the diffusion of Li⁺ through the surface film (R_f) as a result of the decomposition of the electrolyte at high voltages. The semicircle in the medium-frequency region relates to a charge transfer process (R_{ct}). Obviously, as shown in Fig. 3e, both cathodes show no significant difference in film

resistance, but there is significant decrease in the charge transfer resistance of NCM811@LGO, which may be correlated with the stabilized electrode surface. After 100 cycles (Fig. 3f), the electrode interface resistance of NCM811 ($R_f + R_{ct}$) intensively increases and the diagonal line in the low frequency region disappears, revealing that the severe structural degradation results in extremely slow charge transfer kinetics and a sluggish Li⁺ ion diffusion process. Interestingly, the NCM811@LGO cathode can maintain excellent structural stability, as a result of the overall structural modification, which can effectively mitigate the deterioration of the electrode structure and inhibit the sharp increase in interfacial resistance during high-voltage cycling.

With a stabilized structure, the rate performance of a cathode can be reflected in the Li⁺ ion diffusion kinetics, which are highly affected by the degree of channel order and the diffusion energy barriers in the crystal structure. For this purpose, the rate capabilities of the cathodes were investigated at varied current rates. Both cathodes present a similar discharge capacity at a low rate of 0.1C (Fig. 3g), but NCM811@LGO delivers significantly larger discharge capacities compared to NCM811 upon increasing the rate from 0.2C to 2C, which demonstrates that NCM811@LGO displays excellent rate capabilities at a high rate current. Dominated by the electrochemical polarization associated with sluggish Li⁺ ion diffusion kinetics, the significant changes in the charge/discharge profiles indicate that the electrochemical properties of

NCM811 show rapid decay in comparison with NCM811@LGO at increased current rates (Fig. S7a and S7b†). To further clarify the ion diffusion kinetics in the cathode materials, galvanostatic intermittent titration technique (GITT) measurements (see Fig. S7c and S7d†) were carried out to evaluate Li^+ ion diffusion during the charging process,^{45,46} and the diffusion coefficients can be calculated from the relevant formula (see eqn (S1) in the ESI†). Fig. 3h clearly shows that NCM811@LGO displays higher Li^+ ion diffusion coefficients during the charging process compared with NCM811, which is a benefit of the positive effects of Ge-doping, improving diffusion channel order and reducing diffusion energy barriers in NCM811 (see the following section).

3.3. The modeling and calculation of phase transitions and Li^+ diffusion in Ge-doped LiNiO_2

As one of the $\text{LiNi}_{1-x}\text{M}_x\text{O}_2$ compounds derived from LiNiO_2 , the resulting $\text{LiNi}_{0.82}\text{Co}_{0.12}\text{Mn}_{0.06}\text{O}_2$ cathode has similar phase transitions and a similar Li^+ diffusion process to the parent LiNiO_2 . Here, LiNiO_2 is utilized as a model to simplify simulations. The highly delithiated Ni-rich oxide (NiO_2) is thermodynamic meta-stable when charged to a high voltage (>4.3 V), and easily undergoes phase transitions from layered NiO_2 to spinel-like NiO_2 , and then to a NiO phase under further Ni^{2+} ion migration (Fig. 4a).^{47,48} Here, we employ a recently developed stochastic surface walking (SSW) method, integrated with density functional theory (DFT), for crystal sampling to clarify the mechanism of this phase transition. Notably, the resultant structure from the phase transition is highly dependent on the degree of cation mixing,^{6,49} and a spinel-like phase could be considered as an initial degraded structure of the layer structure with lower amounts of cation mixing. Here, a SSW pathway was employed to sample the lowest energy pathway from layered NiO_2 to spinel-like NiO_2 . The structural transition from layered NiO_2 to spinel-like NiO_2 contains three steps and two key

intermediate structures, as shown in Fig. 4b. In the first step (layer to intermediate 1), Ni_{mg} rises from the basal layer of NiO_2 to the interlayer spacing, leaving a Ni vacancy in the bottom NiO_2 layer. In transition state 1 (TS1), Ni_{mg} is located on one side of the O plane of the NiO_2 sandwich layer, while all the bonds of Ni_{mg} with another side O plane undergo bond breaking. Due to the significant structural change causing a large overall barrier of 0.64 eV f.u.⁻¹ (2.56 eV per cell), this step belongs to the rate-determining step of the layer-to-spinel phase transition. In the subsequent step (intermediate 1 to intermediate 2), Ni_{mg} migrates by ~ 2.5 Å, which is accompanied by the shearing movement of NiO_2 basal layers. After this, Ni_{mg} is located to the upper-left of the Ni vacancy in the interlayer spacing. This step is kinetically facilitative, with a shadow transition barrier of 0.29 eV f.u.⁻¹ relative to intermediate 1. In the final step, Ni_{mg} migrates from an A hollow site in the bottom NiO_2 layer to a B site, accompanied by a small shearing movement of the NiO_2 basal layers. In TS3, Ni_{mg} is located at the lattice O bridge site between A and B sites, leading to a decrease in the coordination number of Ni_{mg} from 6 (intermediate 2) to 5 (TS3). This step has a barrier of 0.17 eV f.u.⁻¹. To consider the influence of the doped Ge atoms on the phase transition kinetics, we investigate the phase transition kinetics in Ge-doped NiO_2 , where one Ni atom in the unit cell is replaced by a Ge atom. Our calculations show that the overall transition barrier is 0.72 eV f.u.⁻¹ (2.88 eV per cell), which is 0.08 eV f.u.⁻¹ higher than that of pure NiO_2 , indicating that phase transition is effectively hindered by Ge doping to increase the migration barrier for nearby Ni atoms. The calculation results reveal that Ge-doping has a remarkable effect, suppressing phase transitions in the Ni-rich cathode to alleviate structural degradation from a layer to spinel-like/rock-salt phase transition and enabling excellent cycling stability, which is very consistent with the experimental results (Fig. 3a–d).

Li -ion diffusion is an important requirement for obtaining high power density and fast charge/discharge properties in cathode materials for LIBs. To understand the effects of Ge-doping on Li^+ diffusion, we calculate the Li hopping energy barrier from one Li octahedral site to another vacant Li octahedral site nearby an O-to-O pathway in the NiO_2 and Ge-doped NiO_2 model. To compute the effects of Li occupancy on the diffusion profile, we created three representative Li vacancy models: (i) a single Li vacancy (LiNiO_2 , Fig. 5a and b); (ii) a half Li vacancy ($\text{Li}_{0.5}\text{NiO}_2$); and (iii) a full Li vacancy with no Li retained (NiO_2), and the Li hopping energy barriers were investigated. Surprisingly, Ge-doping can extensively decrease the Li hopping energy. As shown in Fig. 5c, the Li diffusion barrier in Ge-doped LiNiO_2 is 0.49 eV, which is 0.03 eV lower than in LiNiO_2 (0.52 eV). Notably, according to the Arrhenius equation (see the detailed discussion in the ESI†), if the diffusion barrier is reduced by 0.03 eV, this means that the Li^+ diffusion rate in Ge-doped LiNiO_2 would be 3.21 times faster than in a pristine sample. In $\text{Li}_{0.5}\text{NiO}_2$, the Li^+ diffusion barrier in the Ge-doped sample is 0.22 eV, while the pristine sample barrier is slightly higher (0.31 eV). For NiO_2 , the barrier is 0.62 eV in the Ge-doped sample and 0.67 eV in the pristine sample. Therefore, we suggest that the net Li^+ diffusion rates in

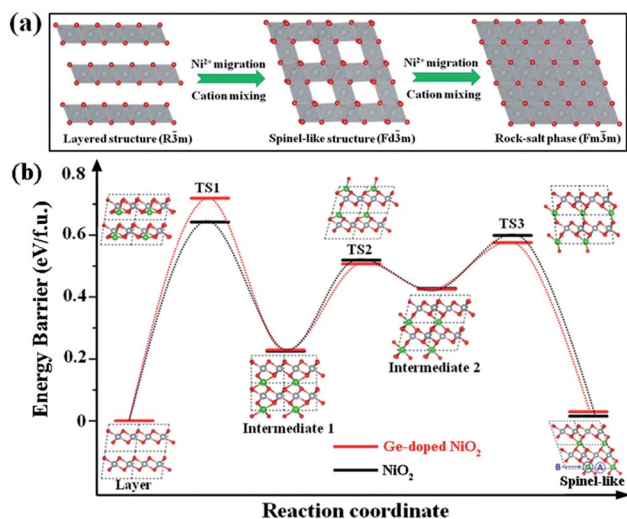


Fig. 4 (a) The phase transitions of highly delithiated Ni-rich oxide (NiO_2). (b) Energy barrier profiles for the phase transition from a layer to a spinel-like structure in Ge-doped NiO_2 and pure NiO_2 .

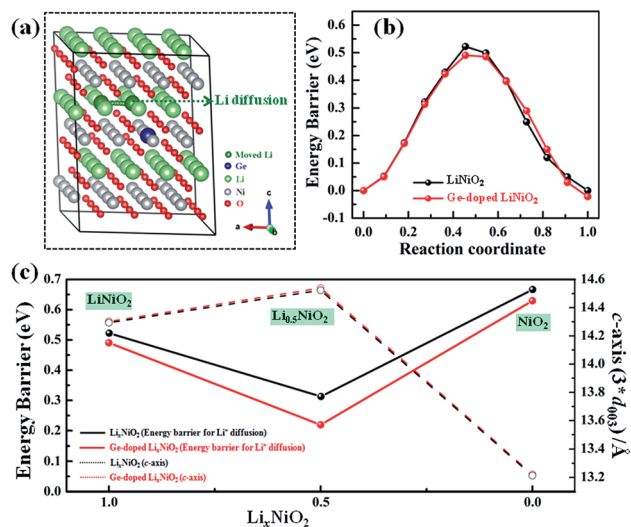


Fig. 5 (a) Li^+ diffusion paths in an ideal layered structural model of Ge-doped LiNiO_2 . (b) The Li^+ diffusion energy barriers of LiNiO_2 and Ge-doped LiNiO_2 in an initial delithiated state. (c) The Li^+ diffusion energy barriers and interlayer distances for Li_xNiO_2 and Ge-doped Li_xNiO_2 in different delithiated states.

materials minutely doped with Ge can extensively promote the diffusion kinetics rather than slow down diffusion, which is found in other reported doping materials.⁵⁰ In addition, the interlayer distances are strongly dependent on the Li content in Li_xNiO_2 , and $\text{Li}_{0.5}\text{NiO}_2$ has increased interlayer distances and a lower energy barrier compared with LiNiO_2 and NiO_2 , which facilitates Li^+ diffusion.⁵¹ Our calculations rationalize the experimental observations that the modified Ni-rich cathode (integrating coating with Ge-doping) has faster Li^+ diffusion kinetics and a superior rate capacity compared with NCM811 (Fig. 3e and f).

3.4. Structural studies of cycled cathodes

The Ni-rich cathode during high-voltage cycling generally suffers severe structure degradation from an initial layer phase ($R\bar{3}m$) to a spinel phase ($Fd\bar{3}m$) and eventually to a rock-salt phase ($Fm\bar{3}m$). To further verify the influence of overall structural modification integrated with surface coating and bulk doping on the electrode structural evolution upon high-voltage cycling, the morphologies and surface/interface micro-regional structures of cycled cathodes were investigated *via* SEM and TEM. As shown in Fig. 6a, the secondary spherical particles in NCM811 suffer severe structural pulverization with the generation of cracks.^{52,53} More seriously for the primary particles in NCM811 (Fig. 6c), a thick SEI film triggered by serious electrode/electrolyte side reactions is formed on the active surface, and the initial layered structure is substantially transformed into a rock-salt $Fm\bar{3}m$ phase, identified through FFT imaging.^{28,29} The severe structural change is responsible for increasing the impedance of the electrode (Fig. 3f), resulting in the deterioration of the electrochemical performance (Fig. 3). As expected, the surface morphology of NCM811@LGO (Fig. 6b) is well maintained without obvious changes after high-voltage cycling.

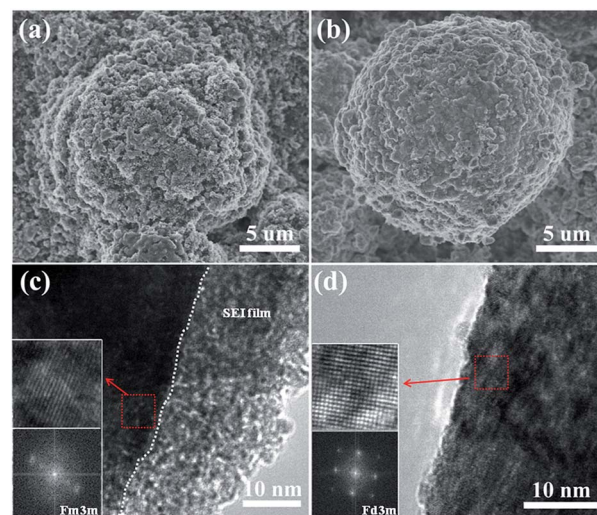


Fig. 6 SEM and TEM images of (a, c) NCM811 and (b, d) NCM811@LGO cathodes after 100 cycles.

Notably, a spinel-like $Fd\bar{3}m$ phase,^{6,54} rather than a rock-salt phase, is clearly observed on the surfaces of the primary particles of NCM811@LGO (Fig. 6d), implying that overall structural modification can efficiently inhibit decomposition from the electrolyte and alleviate structural degradation from a layer phase to a rock-salt phase. This enhanced structural stability is attributed to synergistic effects from Li_2GeO_3 coating and Ge-doping on suppressing phase transitions in the Ni-rich cathode. The Li_2GeO_3 coating inhibits adverse interfacial side reactions at the electrode/electrolyte interface, enhancing the surface stability of the cathode at high voltage, and Ge-doping alleviates structural degradation from a layer phase to a rock-salt phase, as suggested by the first principle calculations. As a result, the suppressed phase transition intensely ameliorates the deterioration of the electrochemical performance of the Ni-rich cathode during high-voltage cycling.

4. Conclusions

In summary, we integrated Li_2GeO_3 coating and gradient Ge-doping in a cathode *via* fusing a coating onto a layered Ni-rich cathode under high-temperature annealing. The modified Ni-rich cathode promotes surface/interface and bulk structural stability and enables excellent cycling stability and superior rate capabilities compared with a pristine cathode at high voltage. The enhanced electrochemical performance is highly associated with the overall structural modification from surface to bulk: the Li_2GeO_3 coating inhibits adverse interfacial side reactions at the electrode/electrolyte interface, enhancing the surface stability of the cathode, while Ge-doping significantly suppresses cation mixing. Powerfully supported by combining experimental results with first principle calculations, it is found that Ge-doping increases the energy barriers for phase transitions in the Ni-rich cathode to alleviate structural degradation from a layer phase to a spinel-like/rock-salt phase, while simultaneously dramatically reducing the diffusion kinetics

barrier, which facilitates Li⁺ diffusion at high-rate currents. The present work provides insights into heterogeneous interface regulation and offers new ideas for the rational design of advanced cathode materials for high-performance LIBs.

Conflicts of interest

There are no conflicts to declare.

Acknowledgements

This work was supported by the National Natural Science Foundation of China (Grant No. 21805179), and the Doctoral Scientific Research Foundation of Shaanxi University of Science and Technology (2016QNBj-09). S.-C. Zhu is supported by the NSFC (Grant No.21703004).

Notes and references

- M. Armand and J. M. Tarascon, *Nature*, 2008, **451**, 652–657.
- J. B. Goodenough and Y. Kim, *Chem. Mater.*, 2010, **22**, 587–603.
- J. S. Weaving, F. Coowar, D. A. Teagle, J. Cullen, V. Dass, P. Bindin, R. Green and W. J. Macklin, *J. Power Sources*, 2001, **97–98**, 733–735.
- W. D. Li, B. H. Song and A. Manthiram, *Chem. Soc. Rev.*, 2017, **46**, 3006–3059.
- F. Schipper, E. M. Erickson, C. Erk, J. Y. Shin, F. F. Chesneau and D. Aurbach, *J. Electrochem. Soc.*, 2017, **164**, A6220–A6228.
- W. Liu, P. Oh, X. Liu, M. J. Lee, W. Cho, S. Chae, Y. Kim and J. Cho, *Angew. Chem., Int. Ed.*, 2015, **54**, 4440–4457.
- J. H. Shim, C. Y. Kim, S. W. Cho, A. Missiul, J. K. Kim, Y. J. Ahn and S. H. Lee, *Electrochim. Acta*, 2014, **138**, 15–21.
- S. M. Bak, K. W. Nam, W. Chang, X. Q. Yu, E. Hu, S. Hwang, E. A. Stach, K. B. Kim, K. Y. Chung and X. Q. Yang, *Chem. Mater.*, 2013, **25**, 337–351.
- P. F. Yan, J. M. Zheng, M. Gu, J. Xiao, J. G. Zhang and C. M. Wang, *Nat. Commun.*, 2017, **8**, 14101.
- H. H. Ryu, K. J. Park, C. S. Yoon and Y. K. Sun, *Chem. Mater.*, 2018, **30**, 1155–1163.
- L. F. Zou, W. G. Zhao, Z. Y. Liu, H. P. Jia, J. M. Zheng, G. F. Wang, Y. Yang, J. G. Zhang and C. M. Wang, *ACS Energy Lett.*, 2018, **3**, 2433–2440.
- H. H. Sun and A. Manthiram, *Chem. Mater.*, 2017, **29**, 8486–8493.
- S. Hwang, S. M. Kim, S. M. Bak, K. Y. Chung and W. Chang, *Chem. Mater.*, 2015, **27**, 6044–6052.
- Z. F. Tang, J. J. Bao, Q. X. Du, Y. Shao, M. H. Gao, B. K. Zou and C. H. Chen, *ACS Appl. Mater. Interfaces*, 2016, **8**, 34879–34887.
- H. Kim, S. Lee, H. Cho, J. Kim, J. Lee, S. Park, S. H. Joo, S. H. Kim, Y. G. Cho, H. K. Song, S. K. Kwak and J. Cho, *Adv. Mater.*, 2016, **28**, 4705–4712.
- J. Yang and Y. Y. Xia, *J. Electrochem. Soc.*, 2016, **163**, A2665–A2672.
- X. H. Xiong, Z. X. Wang, H. J. Guo, Q. Zhang and X. H. Li, *J. Mater. Chem. A*, 2013, **1**, 1284–1288.
- S. U. Woo, C. S. Yoon, K. Amine, I. Belharouak and Y. K. Sun, *J. Electrochem. Soc.*, 2007, **154**, A1005–A1009.
- J. Eom, K. S. Ryu and J. Cho, *J. Electrochem. Soc.*, 2008, **155**, A228–A233.
- H. Gao, X. Q. Zeng, Y. X. Hu, V. Tileli, L. X. Li, Y. Ren, X. B. Meng, F. Maglia, P. Lamp, S. J. Kim, K. Amine and Z. H. Chen, *ACS Appl. Energy Mater.*, 2018, **1**, 2254–2260.
- Y. Y. Wang, Y. Y. Sun, S. Liu, G. R. Li and X. P. Gao, *ACS Appl. Energy Mater.*, 2018, **1**, 3881–3889.
- J. Ahn, J. H. Kim, B. W. Cho, K. Y. Chung, S. Kim, J. W. Choi and S. H. Oh, *Nano Lett.*, 2017, **17**, 7869–7877.
- J. Yang, M. Y. Hou, S. Haller, Y. G. Wang, C. X. Wang and Y. Y. Xia, *Electrochim. Acta*, 2016, **189**, 101–110.
- T. Chen, X. Li, H. Wang, X. Yan, L. Wang, B. W. Deng, W. J. Ge and M. Z. Qu, *J. Power Sources*, 2018, **374**, 1–11.
- J. Yang and Y. Y. Xia, *ACS Appl. Mater. Interfaces*, 2016, **8**, 1297–1308.
- K. Liu, Q. Q. Zhang, S. Dai, W. Li, X. J. Liu, F. Ding and J. L. Zhang, *ACS Appl. Mater. Interfaces*, 2018, **10**, 34153–34162.
- P. F. Yan, J. M. Zheng, J. Liu, B. Q. Wang, X. P. Cheng, Y. F. Zhang, X. L. Sun, C. M. Wang and J. G. Zhang, *Nat. Energy*, 2018, **3**, 600–605.
- Y. Cho, P. Oh and J. Cho, *Nano Lett.*, 2013, **13**, 1145–1152.
- H. Kim, M. G. Kim, H. Y. Jeong, H. Nam and J. Cho, *Nano Lett.*, 2015, **15**, 2111–2119.
- S. C. Zhu, S. H. Xie and Z. P. Liu, *J. Phys. Chem. Lett.*, 2014, **5**, 3162–3168.
- S. C. Zhu, S. H. Xie and Z. P. Liu, *J. Am. Chem. Soc.*, 2015, **137**, 11532–11539.
- Y. F. Li, S. C. Zhu and Z. P. Liu, *J. Am. Chem. Soc.*, 2016, **138**, 5371–5379.
- S. C. Zhu, Q. Hu, W. L. Mao, H. K. Mao and H. Sheng, *J. Am. Chem. Soc.*, 2017, **139**, 12129–12132.
- X. J. Zhang and Z. P. Liu, *J. Chem. Theory Comput.*, 2015, **11**, 4885–4894.
- P. E. Blöchl, *Phys. Rev. B: Condens. Matter Mater. Phys.*, 1994, **50**, 17953–17979.
- J. P. Perdew, K. Burke and M. Ernzerhof, *Phys. Rev. Lett.*, 1996, **77**, 3865–3868.
- H. J. Monkhorst and J. D. Pack, *Phys. Rev. B: Solid State*, 1976, **13**, 5188–5192.
- J. Klimeš, D. R. Bowler and A. Michaelides, *Phys. Rev. B: Condens. Matter Mater. Phys.*, 2011, **83**, 195131.
- C. C. Zhang, M. M. Liu, G. J. Pan, S. Y. Liu, D. Liu, C. G. Chen, J. M. Su, T. Huang and A. S. Yu, *ACS Appl. Energy Mater.*, 2018, **1**, 4374–4384.
- P. P. Jing, P. F. Wang, M. T. Liu, W. S. Gao, Y. F. Cui, Z. Wang and Y. P. Pu, *J. Alloys Compd.*, 2019, **774**, 236–243.
- H. L. Li, X. Wei, P. H. Yang, Y. B. Ren, S. B. Wang, Y. L. Xing and S. C. Zhang, *Electrochim. Acta*, 2018, **261**, 86–95.
- J. C. Zhang, Z. Z. Yang, R. Gao, L. Gu, Z. B. Hu and X. F. Liu, *ACS Appl. Mater. Interfaces*, 2017, **9**, 29794–29803.
- C. L. Xu, W. Xiang, Z. G. Wu, Y. D. Xu, Y. C. Li, M. Z. Chen, X. D. Guo, G. P. Lv, J. Zhang and B. H. Zhong, *ACS Appl. Mater. Interfaces*, 2018, **10**, 27821–27830.

- 44 Y. Cho, S. Lee, Y. Lee, T. Hong and J. Cho, *Adv. Energy Mater.*, 2011, **1**, 821–828.
- 45 Y. S. Bai, X. Y. Wang, X. Y. Zhang, H. B. Shu, X. K. Yang, B. A. Hu, Q. L. Wei, H. Wu and Y. F. Song, *Electrochim. Acta*, 2013, **109**, 355–364.
- 46 V. D. V. Anton, J. Bhattacharya and A. A. Belak, *Acc. Chem. Res.*, 2013, **46**, 1216–1225.
- 47 S. Muto, Y. Sasano, K. Tatsumi, T. Sasaki, K. Horibuchi, Y. Takeuchi and Y. Ukyo, *J. Electrochem. Soc.*, 2009, **156**, A371–A377.
- 48 K. W. Nam, S. M. Bak, E. Hu, X. Yu, Y. Zhou, X. Wang, L. Wu, Y. Zhu, K. Y. Chung and X. Q. Yang, *Adv. Funct. Mater.*, 2013, **23**, 1047–1063.
- 49 S. K. Jung, H. Gwon, J. Hong, K. Y. Park, D. H. Seo, H. Kim, J. Hyun, W. Yang and K. Kang, *Adv. Energy Mater.*, 2014, **4**, 1300787.
- 50 M. Dixit, B. Markovsky, D. Aurbach and D. T. Major, *J. Electrochem. Soc.*, 2017, **164**, A6359–A6365.
- 51 W. He, D. D. Yuan, J. F. Qian, X. P. Ai, H. X. Yang and Y. L. Cao, *J. Mater. Chem. A*, 2013, **1**, 11397–11403.
- 52 E. J. Lee, Z. H. Chen, H. J. Noh, S. C. Nam, S. Kang, D. H. Kim, K. Amine and Y. K. Sun, *Nano Lett.*, 2014, **14**, 4873–4880.
- 53 J. M. Lim, T. Hwang, D. Kim, M. S. Park, K. Cho and M. Cho, *Sci. Rep.*, 2017, **7**, 39669.
- 54 S. K. Jung, H. Gwon, J. Hong, K. Y. Park, D. H. Seo, H. Kim, J. Hyun, W. Yang and K. Kang, *Adv. Energy Mater.*, 2014, **4**, 1300787–1300793.